



Cite this: *Phys. Chem. Chem. Phys.*,  
2024, 26, 10610

## Homochiral vs. heterochiral preference in chiral self-recognition of cyclic diols†

Jennifer Dupont,<sup>a</sup> Beppo Hartwig,<sup>ib</sup> Katia Le Barbu-Debus,<sup>id</sup> Valeria Lepere,<sup>id</sup> Regis Guillot,<sup>id</sup> Martin A. Suhm<sup>id</sup> and Anne Zehnacker<sup>id</sup>\*

The structure and clustering propensity of a chiral derivative of *cis*-1,2-cyclohexanediol, namely, 1-phenyl-*cis*-1,2-cyclohexanediol (*cis*-PCD), has been studied under supersonic expansion conditions by combining laser spectroscopy with quantum chemistry calculations. The presence of the phenyl substituent induces conformational locking relative to *cis*-1,2-cyclohexanediol (*cis*-CD), and only one conformer of the bare molecule is observed by both Raman and IR-UV double resonance spectroscopy. The homochiral preference inferred for the dimer formation at low enough temperature is in line with the formation of a conglomerate in the solid state. The change in clustering propensity in *cis*-PCD relative to *trans*-1,2-cyclohexanediol (*trans*-CD), which shows heterochiral preference, is explained by the presence of the phenyl substituent rather than the effect of *cis-trans* isomerism. Indeed the transiently chiral *cis*-CD also forms preferentially heterodimers, whose structure is very close to that of the corresponding *trans*-CD dimer.

Received 25th January 2024,  
Accepted 8th March 2024

DOI: 10.1039/d4cp00351a

rsc.li/pccp

### Introduction

Life is characterised by a strong homochiral preference: all the proteogenic amino acids are of identical absolute configuration, and so are all the sugars, and the reason for the initial dissymmetry between the two enantiomers is still under debate.<sup>1–3</sup> It is commonly admitted that non-covalent interactions play a major role in shaping the homochirality of biomolecules. For example the helical structure of an all-*L* polyalanine peptide is disrupted by the mere presence of a *D* residue.<sup>4</sup> The solid state of chiral molecules contrasts with biomolecules as most of the racemic mixtures crystallise in the form of racemates, in which the unit cell contains both enantiomers that are intimately mixed.<sup>5</sup> Racemic mixtures that crystallise as conglomerate are scarcer. They are estimated to form about 5–10% of the total racemic crystals, although DFT-based calculations suggest that thermodynamic conglomerate abundance should actually reach 20% or more.<sup>6,7</sup> In these

conglomerates, separate crystals of the two enantiomers are formed, which can be further manually separated. An example of such conglomerates is the tartrate salts at the basis of the discovery of chirality by Pasteur.<sup>8</sup>

Several attempts have been reported to assess the homochiral or heterochiral preference in molecular pairs isolated in the gas phase.<sup>9,10</sup> The gas-phase dimer structure often differs from that observed in the solid, because the isolated dimer tries to optimise the number of hydrogen bonds. In particular, alcohols or substituted alcohols have been the subjects of many studies, for example the 1-indanol<sup>11</sup> or fluoroethanol dimer.<sup>12</sup> Bifunctional compounds are especially interesting in this respect as they provide more anchoring points that are expected to favour chiral discrimination.<sup>13</sup> Examples include systems with permanent chirality like the methyl lactate<sup>14–16</sup> or the protonated 1-amino-2-indanol dimers<sup>17</sup> or systems showing transient chirality like vicinal diols or aminoalcohols. In the latter systems, the two enantiomers are interconverted by torsion around a CC bond. Tunnelling between the two enantiomers manifests itself by the splitting of the transitions observed in microwave spectroscopy.<sup>18</sup> The torsion can be blocked by dimer formation, which allows observing both homochiral and heterochiral dimers, with a preference for heterochiral pairing in the case of the 1,2-ethanediol dimer, whose preferred structure is achiral with *S*<sub>4</sub> symmetry.<sup>19</sup> In contrast, the aminoethanol dimer shows homochiral preference.<sup>20</sup> Trends for homochiral aggregation are also observed for transiently chiral substituted alcohols such as the trifluoroethanol dimer or large clusters of phenyl-methanol, up to the tetramer.<sup>21,22</sup>

<sup>a</sup> Institut des Sciences Moléculaires d'Orsay (ISMO), CNRS, rue André Rivière, Université Paris-Saclay, F-91405 Orsay, France.

E-mail: anne.zehnacker-rentien@universite-paris-saclay.fr

<sup>b</sup> Institut für Physikalische Chemie, Georg-August-Universität Göttingen, Tammannstr. 6, 37077 Göttingen, Germany

<sup>c</sup> Institut de Chimie Moléculaire et des Matériaux d'Orsay (ICMMO), 17 Av. des Sciences Université Paris-Saclay, F-91405 Orsay, France

† Electronic supplementary information (ESI) available. CCDC 2277624. For ESI and crystallographic data in CIF or other electronic format see DOI: <https://doi.org/10.1039/d4cp00351a>



Information has been gained recently on the chiral preference in the jet-cooled dimer of 1,2-ethanediol, by comparison with one of its cyclohexane analogues, the permanently chiral *trans*-1,2-cyclohexanediol (*trans*-CD).<sup>23</sup> *trans*-CD shows heterochiral pairing preference in the gas phase due to the formation of a strongly bound dimer optimising the number of hydrogen bonds. The isolated 1,2-ethanediol dimers form the same hydrogen-bond pattern, hence the same heterochiral preference in the gas phase. Heterochiral preference is also observed in the *trans*-CD solid, which is a racemate.<sup>24</sup>

In contrast to *trans*-CD, *cis*-1,2-cyclohexanediol (*cis*-CD) is only transiently chiral because of the plane of symmetry that intersects the C<sub>1</sub>C<sub>2</sub> bond when the carbon skeleton is made planar. Moreover, the *cis* geometry of the substituents will influence the strength of the intramolecular hydrogen bond relative to *trans*-1,2-cyclohexanediol. *trans* CD is energetically favoured by 1.9 kJ mol<sup>-1</sup> in terms of zero-point-corrected energy at the B3LYP-D3(BJ,abc)/ma-def2-TZVP level of theory. Adding a phenyl substituent results in 1-phenyl-*cis*-1,2-cyclohexanediol (*cis*-PCD) that is permanently chiral. Dimer formation and chiral preference are expected to differ between *trans*-CD, *cis*-CD and *cis*-PCD, and may be influenced by the competition between intra- and intermolecular hydrogen bonds formation.<sup>12,25</sup> On the other hand, the aromatic  $\pi$ -system adds both steric hindrance and dispersion interactions in *cis*-PCD and acts as an efficient hydrogen bond acceptor.<sup>26</sup> These factors result in a wealth of expected hydrogen bond patterns in the aromatic dimer.

Here, we report the spectroscopic properties of *cis*-PCD and its dimers under supersonic expansion conditions, as studied by resonance-enhanced multi-photon ionisation (REMPI), Raman scattering, and conformer specific vibrational spectroscopy. The vibrational spectra of the homochiral and heterochiral dimers obtained by double resonance IR-UV spectroscopy are interpreted with the help of density functional theory (DFT) calculations to shed light on the diastereomeric preference in *cis*-PCD. The interaction patterns observed in the gas phase are compared to those existing in the solid. The structures found thereby are compared to the non-aromatic systems *cis*- and *trans*-CD.

## Experimental and theoretical methods

### 1. Experimental methods

*cis*-PCD (99%) was purchased from Santa Cruz Biotechnology (USA). *cis*-CD (99%) was bought from Sigma Aldrich. Both samples were used without further purification.

The Raman spectroscopy results were obtained using a slit jet at the Institut für Physikalische Chemie. In the following, we will give a description of the measurement conditions for *cis*-PCD. When conditions differ between *cis*-PCD and *cis*-CD, the values for the latter will be given in parentheses. Pure He was used as a carrier gas and continuously expanded at a stagnation pressure of 0.4 bar (1.4 bar for *cis*-CD) into low vacuum ( $\sim$  a few 10<sup>-1</sup> mbar). Raman scattering was obtained from a 532 nm cw laser operated at 24 W, with the expansion being irradiated orthogonally 1 mm (1.25 mm for *cis*-CD)

downstream of the nozzle. The scattered light was collected by a photo lens perpendicular to the laser, focussed towards a Czerny–Turner-monochromator and detected by a LN2 cooled CCD camera. An exposure time of 4 min was used with 18 such exposures being averaged (5 for *cis*-CD) to yield the experimental spectrum. The spectrum was calibrated using Ne lines. The vapour pressure of the diol was enhanced in a heatable saturator kept at 395 K (365 K for *cis*-CD) with the following tubing and nozzle being heated to 425 K (395 K for *cis*-CD) to avoid condensation.<sup>27</sup>

The electronic and vibrational spectroscopy results for *cis*-PCD were obtained using a pinhole jet at ISMO. The pulsed supersonic beam was produced by expanding 2 bar of helium seeded with the enantiopure or racemic *cis*-PCD into high vacuum ( $\sim$ 10<sup>-6</sup> mbar) through a 200  $\mu$ m pulsed nozzle (General Valve – Parker).<sup>28</sup> *cis*-PCD was put in an oven just prior the expansion and heated at 365 K for the study of the monomer and 400 K for that of the dimer. Mass-resolved electronic spectra were obtained using one-colour resonance-enhanced two-photon ionisation (RE2PI). The UV source (0.02 cm<sup>-1</sup> resolution) was generated by doubling the output of a dye laser (Sirah equipped with C540A dye) pumped by the second harmonic of a Nd:YAG laser (Quanta Ray, Spectra Physics). The UV laser beam was mildly focused by a 1 m focal length lens and crossed the skimmed supersonic beam (skimmer of 500  $\mu$ m diameter) in the interaction zone of a linear time-of-flight (TOF) mass spectrometer (Jordan, one-meter length). The ion signal was detected by a microchannel plate detector (RM Jordan, 25 mm diameter), averaged by an oscilloscope (Lecroy wavesurfer), and processed through a personal computer.

Vibrational spectra were recorded using the IR-UV double resonance method.<sup>29,30</sup> A slightly focused (0.5 m focal length lens) IR laser beam (OPO/OPA – Laser Vision – 3 cm<sup>-1</sup> resolution) was counter-propagated relative to the UV laser beam and superimposed to it in the source region. After fixing the UV probe laser on selected vibronic transitions of the electronic spectrum, the wavelength of the IR pump laser was scanned in the 3  $\mu$ m region. The IR absorption was then detected as a depletion of the UV-induced ion signal. The IR pulse was triggered  $\sim$ 80 ns before the UV pulse to record ground-state vibrational spectra. Synchronisation between the lasers was controlled by a homemade gate generator. The IR spectra were recorded resorting to an active baseline scheme, by measuring the difference in ion signal produced by successive UV laser pulses (one without and one with the IR laser pulse present).<sup>31</sup>

X-ray diffraction data for compound *cis*-PCD were collected following the protocol described in the ESI.†

### 2. Theoretical methods

The potential energy surfaces (PES) of the *cis*-PCD monomer, its dimers, and those of *cis*-CD were first explored using the OPLS-2005 force fields with the advanced conformational search implemented in the MacroModel suite, a part of the Schrödinger package.<sup>32</sup> Geometry optimization of the structures found thereby with energy below 21 kJ mol<sup>-1</sup> and vibrational frequencies calculation were performed using the B3LYP functional



combined to the 6-311++G(d,p) basis set,<sup>33</sup> and including D3BJ dispersion corrections.<sup>34,35</sup> The minimum energy monomers resulting from the PES exploration yield the structures that were observed experimentally (*vide infra*). Because the structure of the dimers results from a competition between inter- and intra-molecular hydrogen bonds, their formation depends on multiple factors including crossing energy barriers. For this reason, we also included additional dimer structures that would be above 21 kJ mol<sup>-1</sup> in the exploration or missed with the force field used, for example hydrogen bond patterns observed in similar systems like *trans*-CD. These structures were optimised in the same manner. The vibrational spectra were simulated in the frame of the double harmonic approximation at the same level of theory and the absence of imaginary frequencies was checked for all minima found. The harmonic frequencies were scaled by 0.952 to correct for anharmonicity, functional deficiencies and basis set incompleteness.<sup>36,37</sup>

The relative stability of the different conformers was assessed by comparing their relative zero-point-corrected energies  $\Delta E_0$  and their standard Gibbs free energies  $\Delta G$  (we suppress the standard sign because only differences are relevant in the present work) relative to the most stable conformation at 300 K. Comparison between  $\Delta E_0$  and  $\Delta G$  is especially relevant for dimers, because they are formed at a temperature somewhere between that of the nozzle and the temperature where the expansion is probed. The difference between  $\Delta E_0$  and  $\Delta G$  may be viewed as a rough estimate of the uncertainty in the predicted energy ranking. The deformation energy was calculated as the difference in energy between the structure of the monomer in the complex and that of its most stable form.<sup>25,38,39</sup> The deformation energy mentioned in what follows is the sum of that of the two monomers.

The nature of the first two electronic excited states and the vertical transition energies were calculated at the TD-DFT level at the same level as the ground state, using 4 excited states. The difference in electronic densities was calculated from the cube files generated by the Gaussian software and using the “cubman” facility. The resulting densities were plotted using the VMD software with an isovalue of 0.001. All these calculations were performed with the Gaussian Package (Version 16 Rev. B.01).<sup>40</sup>

For the sake of comparison with previously published work and sensitivity analysis with respect to small computational details like three-body-inclusive dispersion correction and basis set variants, the energies and harmonic frequencies were also calculated at the B3LYP-D3(BJ,abc)/ma-def2-TZVP<sup>41,42</sup> level using the ORCA (version 5.0.3) program package.<sup>43</sup> The theoretical spectra were simulated using the harmonic frequencies scaled by 0.963. Furthermore, a recently proposed empirical model<sup>45</sup> was applied to the *cis*-PCD monomer to account for density functional deficiencies and the missing anharmonicity. Specifically, a correction of  $-146.0$  cm<sup>-1</sup> was used to account for the degree of substitution at the 1,2-diol subunit as well as an additional correction of  $-8$  cm<sup>-1</sup> due to the phenyl group. In the case of the PCD dimers, for which highly anharmonic low-frequency modes are expected, the Gibbs energy calculations were also conducted using the Quasi Rigid Rotor Harmonic

Oscillator (QRRHO) approximation developed by Grimme,<sup>44</sup> as a second measure for the uncertainty involved in such calculations. The results and discussion that follow are based on the B3LYP-D3(BJ,abc)/ma-def2-TZVP calculations, unless specified otherwise. The B3LYP-D3BJ/6-311++G(d,p) results are given in the ESI† as well as the comparison with QRRHO.

## Results and discussion

The molecule under multi-experimental study, *cis*-1-phenylcyclohexane-1,2-diol, as well as *trans*-1,2-cyclohexanediol and *cis*-1,2-cyclohexanediol are shown in Fig. 1.

### 1. *cis*-PCD Monomer

(a) **Experimental spectra.** The Raman spectrum shows two bands, both being down-shifted relative to a free  $\nu(\text{OH})$ , at 3574.0 and 3611.5 cm<sup>-1</sup> (Fig. 2a). These frequencies are typical of OH groups involved in a weak intramolecular OH...O and an OH... $\pi$  interaction, as confirmed by the calculations described below. These results indicate that a single conformer of *cis*-PCD is observed under slit jet conditions.

Fig. 3 shows the  $S_1 \leftarrow S_0$  spectrum of the *cis*-PCD monomer. The strong transition origin at 37766 cm<sup>-1</sup> is followed by a progression built on a low-frequency mode of 28 cm<sup>-1</sup>. The same progression appears in combination with the Herzberg-Teller allowed mode at +528 cm<sup>-1</sup>.

IR-UV double resonance spectra have been recorded by setting the UV probe on all the transitions marked by \* in Fig. 3; that obtained by probing the transition origin is displayed in Fig. 2b. They are identical whatever the probe wavelength, showing unambiguously that only one conformer exists under pinhole jet conditions too. The spectrum shows two bands, both being down-shifted relative to a free  $\nu(\text{OH})$ , at 3575 and 3613 cm<sup>-1</sup>, very close to the Raman spectroscopy values (Fig. 2a).

(b) **Calculated results.** The structure of the monomer depends on the conformation of the cyclohexane ring and that of the hydroxyl substituents. The monomers having the cyclohexane ring in a boat structure are much higher in energy ( $>25$  kJ mol<sup>-1</sup>) than those with a chair structure and will not be discussed further. Similarly, the monomers having the phenyl substituent in axial position are destabilized ( $>13$  kJ mol<sup>-1</sup>) relative to those with the phenyl in equatorial position.

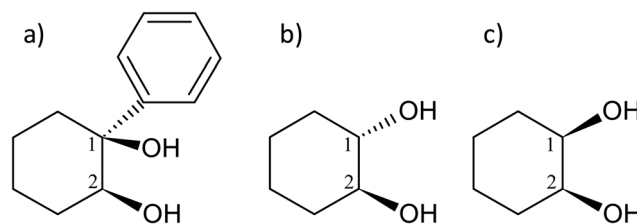
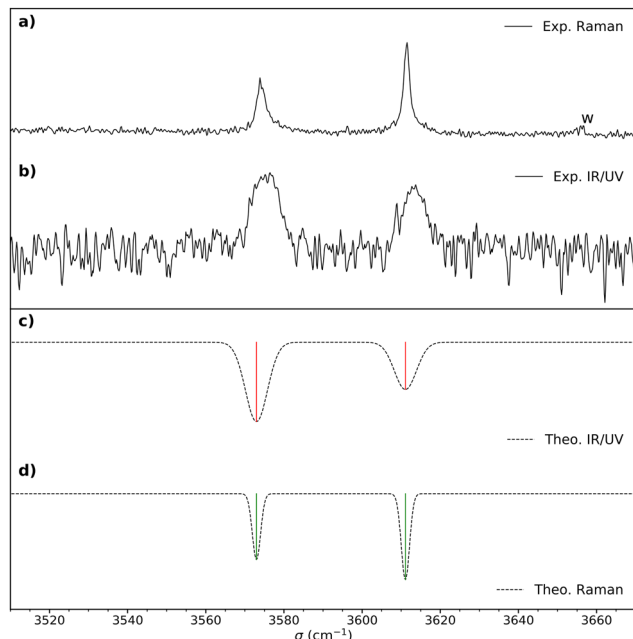


Fig. 1 Scheme and atom numbering for (a) (*S,S*)-(+)-1-phenylcyclohexane-*cis*-1,2-diol (*cis*-PCD) (b) (*1S,2S*)-*trans*-1,2-cyclohexanediol (*trans*-CD) (c) *cis*-1,2-cyclohexanediol (*cis*-CD).





**Fig. 2** (a) Raman spectrum of *cis*-PCD. “w” denotes a water impurity signal. (b) Double resonance spectrum of the monomer obtained by setting the UV probe on the transition origin at  $37766\text{ cm}^{-1}$ . (c) IR spectrum simulated for the most stable structure  $M_1$ , shown in Fig. 4, obtained from the B3LYP-D3(BJ,abc)/ma-def2-TZVP empirically corrected harmonic frequencies. (d) Simulated Raman spectrum obtained from the empirically corrected harmonic B3LYP-D3(BJ,abc)/ma-def2-TZVP frequencies. The computed harmonic frequencies have been corrected by a recently proposed empirical correction model (see text and ref. 46). A Gaussian line profile is assumed with a full width at half maximum of  $4\text{ cm}^{-1}$  and  $1.5\text{ cm}^{-1}$  for the IR/UV and Raman spectra, respectively. Scaled B3LYP-D3(BJ,abc)/ma-def2-TZVP or B3LYP-D3(BJ)/6-311++G(d,p) harmonic frequencies calculations yield similar results.



**Fig. 3** REMPI  $S_1 \leftarrow S_0$  electronic spectrum of the *cis*-PCD monomer obtained by monitoring its mass at  $m/z$  192 as a function of the laser wavenumber. The  $28\text{ cm}^{-1}$  progression is materialised by vertical lines. The IR-UV spectra were recorded by setting the probe on the electronic transitions indicated by \*.



**Fig. 4** Most stable structures of the PCD monomer, together with relative zero-point corrected energy  $\Delta E_0$  and relative Gibbs energy at room-temperature  $\Delta G$ , calculated at the B3LYP-D3(BJ,abc)/ma-def2-TZVP level. The OH...O and OH... $\pi$  hydrogen bonds are shown by red dashed lines.

We are thus left with the three structures shown in Fig. 4, together with their energetics (Gibbs energy  $\Delta G$  and ZPE-corrected energy  $\Delta E_0$ ). Their energetics are summarised in Table S1 of the ESI.† They all show the phenyl and the  $O_2H$  in equatorial position, and the  $O_1H$  in axial position. They all involve a sterically constrained OH...O intramolecular interaction. We shall discuss their energetics in terms of relative Gibbs energies and ZPE-corrected energy  $\Delta E_0$  at the B3LYP-D3(BJ,abc)/ma-def2-TZVP level. The energetics (relative Gibbs energy  $\Delta G$  and ZPE-corrected energy  $\Delta E_0$ ) and geometrical parameters at the B3LYP-D3BJ/6-311G++(d,p) level are listed in Table S2 of the ESI.† These structures will be called M (like monomer) with the index 1 or 2 when the OH on the carbon atom 1 or 2 is acting as a hydrogen bond donor, respectively. Both  $M_1$  and  $M_1'$  show an  $O_1H \cdots O_2$  interaction. They only differ by a rotation of  $O_2H$  that allows a weak  $O_2H \cdots \pi$  interaction to take place in  $M_1$  and not in  $M_1'$ .  $M_1$  is thus stabilised by  $6.7\text{ kJ mol}^{-1}$  relative to  $M_1'$ , in terms of  $\Delta G$ . This value can be taken as an estimation of the OH... $\pi$  interaction energy.  $M_2$  shows a hydrogen bond in the opposite direction, namely, an  $O_2H \cdots O_1$  interaction and is much less stable than  $M_1$  because no OH... $\pi$  interaction is possible in  $M_2$  due to steric reasons. Notwithstanding the difference in hydrogen bond directions, the backbones are very similar in  $M_1'$  and  $M_2$ . The Gibbs energy of  $M_2$  relative to  $M_1$  is  $9.6\text{ kJ mol}^{-1}$ , which allows roughly assessing the difference between  $O_2H \cdots O_1$  and  $O_1H \cdots O_2$  interactions to  $\sim 3\text{ kJ mol}^{-1}$ . The energy barrier for converting  $M_1'$  to  $M_1$  is calculated at  $2.5\text{ kJ mol}^{-1}$  and is overcome in our experimental conditions,<sup>45</sup> therefore only  $M_1$  is expected to be observed. The energy ranking is the same if one considers  $\Delta E_0$  or the values obtained at the B3LYP-D3BJ/6-311G++(d,p) level (see Tables S1 and S2, ESI†), the values obtained with the various approaches differing by less than 10%.

The splitting of the calculated frequencies of  $M_1$  matches well the experimental one, whatever the method used. The empirical scaling model developed for diols also predicts the absolute wavenumbers very well, although *cis*-PCD was not part of the training set.<sup>46</sup>  $\nu(O_1H)$  ( $3574.0$  for the Raman and  $3575$  for the IR-UV results) is much lower than its counterpart in the related structure of *cis*-CD ( $3648\text{ cm}^{-1}$ ),<sup>46</sup> as expected from the presence of an  $O_1H \cdots \pi$  interaction. Moreover, also  $\nu(O_2H)$  ( $3611.5$  for the Raman and  $3613$  for the IR-UV results) is lower in frequency, which points towards a cooperative effect between the two hydrogen bonds, as observed also for intermolecular



hydrogen bonds.<sup>26,47,48</sup> The intramolecular hydrogen bond is hindered and far from linearity ( $\theta(\text{O}_1\text{HO}_2) = 115^\circ$  and  $d(\text{O}_1\text{H}\cdots\text{O}_2) = 2.22 \text{ \AA}$  in  $M_1$ ), which explains the limited downshift of  $\nu(\text{O}_1\text{H})$  compared to intermolecular  $\text{OH}\cdots\text{O}$  interactions.

### (c) Comparison with *cis*- and *trans*-1,2-cyclohexanediol.

The unique structure observed here contrasts with the unsubstituted *cis*-cyclohexane-1,2-diol, which shows three populated conformers below  $10 \text{ kJ mol}^{-1}$  as evidenced by Raman spectroscopy, c6-6, c6-6', and c6-6a in reference,<sup>46</sup> here renamed  $C_1'$ ,  $C_1$ ,  $C_2$  by analogy and for a better comparison.  $C_1'$  is the dominant form and corresponds to  $M_1'$  in *cis*-PCD. Although the experimentally observed conformers  $C_1$ ,  $C_1'$ , and  $C_2$  of *cis*-CD are similar to  $M_1$ ,  $M_1'$ ,  $M_2$  of *cis*-PCD, respectively, the energetic ordering is different. The stability of the first two conformers is inverted due to the possibility of an  $\text{OH}\cdots\pi$  interaction in  $M_1$  and not in  $M_1'$ , which does not intervene in *cis*-CD.<sup>46</sup> The Gibbs energy difference between the two most stable conformers of *cis*-PCD is large ( $6.7 \text{ kJ mol}^{-1}$ ), as is  $\Delta E_0$  ( $7.2 \text{ kJ mol}^{-1}$ ), due to the  $\text{OH}\cdots\pi$  hydrogen bond. This, in addition to the small interconversion barrier ( $2.5 \text{ kJ mol}^{-1}$ ), explains that only  $M_1$  is observed in *cis*-PCD. In both *cis*-CD and *cis*-PCD, one of the hydroxyl substituents is in equatorial and the other one in axial position. In *cis*-PCD, the equatorial position of the bulky phenyl substituent is favoured to decrease the 1-3 diaxial interactions, and the most stable structure has its  $\text{O}_2\text{H}$  group in equatorial and its  $\text{O}_1\text{H}$  in axial position, with an  $\widehat{\text{O}_1\text{HO}_2}$  angle of  $115^\circ$ .

*cis/trans* isomerism also influences the diol structure. The two OH substituents are in equatorial position in *trans*-CD, hence equivalent. Two monomers with a different orientation of the accepting OH are calculated, corresponding to an  $\widehat{\text{O}_1\text{O}_2\text{H}}$  angle of  $145^\circ$  and  $110^\circ$ , respectively ( $M$  and  $M'$  in reference,<sup>23</sup> here renamed  $T'$  and  $T$  for better distinction and analogy), akin to  $M_1'$  and  $M_2$  in *cis*-PCD, notwithstanding the axial or equatorial position. In the absence of other interactions,  $T$  and  $T'$  are almost isoenergetic. They differ in energy by about  $1 \text{ kJ mol}^{-1}$  and their interconversion barrier is of the order of  $4 \text{ kJ mol}^{-1}$ . The two of them are therefore observed under slit jet conditions.<sup>23</sup>

## 2. Dimers

**(a) Electronic spectroscopy of the *cis*-PCD dimer.** Due to the low vapour pressure of *cis*-PCD, slit-jet Raman experiments were out of reach for its dimer. The electronic spectrum of the *cis*-PCD dimer, using either an enantiopure or a racemic mixture, is shown in Fig. 5. Two transitions, namely,  $S_1 \leftarrow S_0$  and  $S_2 \leftarrow S_0$  located on each of the subunits, are expected in this energy range. The  $S_1 \leftarrow S_0$  origin ( $37441 \text{ cm}^{-1}$ ) of the homochiral dimer is downshifted in energy relative to that of the monomer by  $325 \text{ cm}^{-1}$ , a value slightly larger than that observed for other aromatic dimers like the anisole dimer ( $\sim 240 \text{ cm}^{-1}$ ) or the 1-indanol dimer ( $\sim 250 \text{ cm}^{-1}$ ).<sup>11,49</sup> The intense transition origin is followed by low-frequency modes located at 15, 22, 42,  $56 \text{ cm}^{-1}$ . An intense band also appears at  $237 \text{ cm}^{-1}$  from the  $S_1 \leftarrow S_0$  origin, *i.e.*  $-88 \text{ cm}^{-1}$  from the

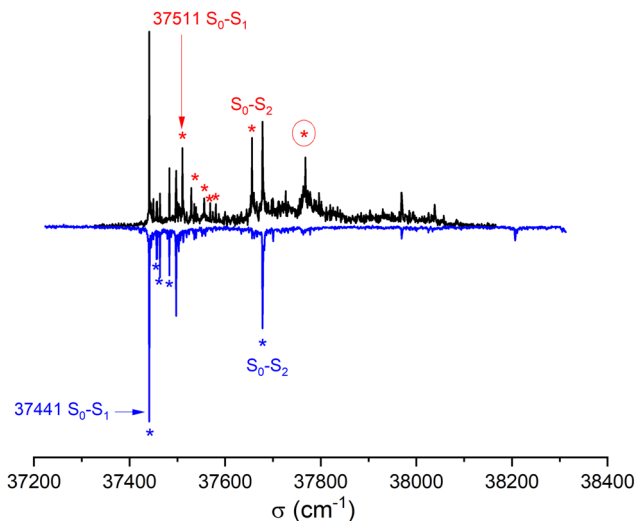


Fig. 5 REMPEI electronic spectrum of the *cis*-PCD dimer for the enantiopure mixture (bottom, blue line) and the racemic sample (top, black line) obtained by monitoring its mass at  $m/z$  384 as a function of the laser wavenumber. The transitions used as a probe for the IR-UV experiments are indicated by asterisks (see text). The numbers give the position of the  $S_1 \leftarrow S_0$  transition origins of the homochiral and heterochiral complexes.

monomer origin. It probably corresponds to the  $S_2 \leftarrow S_0$  origin. Interestingly, only a weak combination band involving the  $22 \text{ cm}^{-1}$  mode is observed, pointing towards different Franck-Condon activity for the  $S_1 \leftarrow S_0$  and  $S_2 \leftarrow S_0$  transitions. The other bands observed in the spectrum correspond to the Herzberg-Teller allowed mode of the benzene ring in  $S_1$  ( $528 \text{ cm}^{-1}$  from the  $S_1 \leftarrow S_0$  origin) or  $S_2$  ( $528 \text{ cm}^{-1}$  from the  $S_2 \leftarrow S_0$  origin). The strong decrease in band intensity at higher energy points towards the onset of non-radiative processes, which were not apparent in the monomer.

The spectrum of racemic *cis*-PCD clearly shows additional bands, which are due to the heterochiral dimer. The downshift of the  $S_1 \leftarrow S_0$  transition origin of the heterochiral dimer ( $37511 \text{ cm}^{-1}$ ) is smaller ( $255 \text{ cm}^{-1}$  from the monomer origin). A low-frequency pattern similar to that of the homochiral dimer is observed near the  $S_1 \leftarrow S_0$  origin, with bands at 18, 45,  $57 \text{ cm}^{-1}$  from the  $S_1 \leftarrow S_0$  origin. An additional weak band appears at  $70 \text{ cm}^{-1}$ . The band tentatively assigned to the  $S_2 \leftarrow S_0$  origin, located at  $145 \text{ cm}^{-1}$  from the  $S_1 \leftarrow S_0$  origin, also shows a larger down shift relative to the monomer than the homochiral dimer ( $110 \text{ cm}^{-1}$ ). The same decrease in band intensity at higher energy is observed as for the homochiral dimer. Still, an intense band is observed at  $+257 \text{ cm}^{-1}$  of the  $S_1 \leftarrow S_0$  origin, a point to which we shall come back later.

**(b) Vibrational spectroscopy of the *cis*-PCD dimer.** IR-UV spectra have been recorded setting the probe on the bands marked by an asterisk in the REMPEI spectra shown in Fig. 5. They are displayed in Fig. 6. The spectrum of the homochiral dimer is identical whatever the band probed (Fig. 6a). It shows four transitions, as expected from the number of  $\nu(\text{OH})$  oscillators, all characteristic of bound OH groups. A congested doublet at  $3554/3563 \text{ cm}^{-1}$  suggests the existence of two weak hydrogen



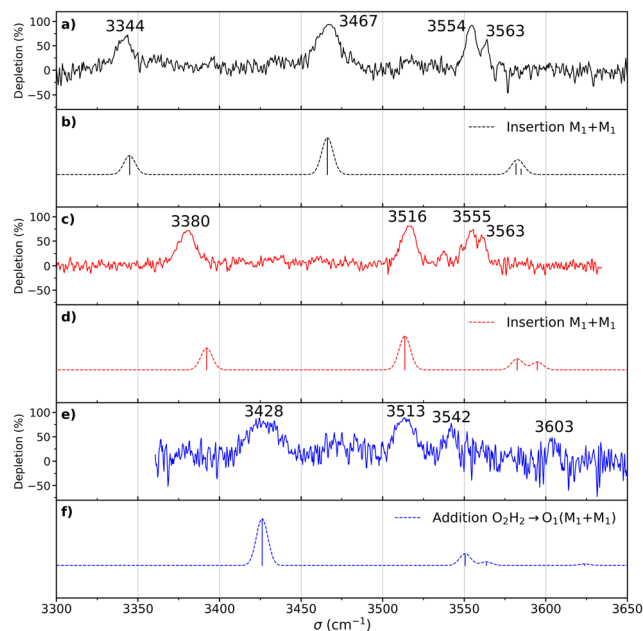


**Fig. 6** (a) Experimental double resonance spectrum of the homochiral dimer recorded by setting the probe on the transition origin at  $37441\text{ cm}^{-1}$ . (b) Simulated spectrum of the most stable structure of the homochiral dimer (insertion  $M_1 + M_1$ ). (c) Experimental spectrum of the heterochiral dimer recorded by setting the probe on the transition origin at  $37511\text{ cm}^{-1}$ . (d) Simulated spectrum of the most stable structure (in terms of  $\Delta E_0$ ) of the heterochiral dimer (insertion  $M_1 + M_1$ ). (e) Experimental spectrum of the heterochiral complex recorded by setting the probe on the transition at  $37768\text{ cm}^{-1}$ . (f) Simulated spectra of the most stable structure (judging by  $\Delta G$  at 300 K) of the heterochiral dimer (addition  $\text{O}_2\text{H}_2 \cdots \text{O}_1(M_1 + M_1)$ ). The theoretical spectra have been simulated using the scaled harmonic frequencies (scaling factor of 0.963) calculated at the B3LYP-D3(BJ,abc)/ma-def2-TZVP level and convoluted by a Gaussian profile ( $4\text{ cm}^{-1}$  FWHM).

bonds. Two strongly shifted transitions, at  $3344$  and  $3467\text{ cm}^{-1}$  are the signature of strong intermolecular hydrogen bonds.

The most stable calculated homochiral structure (Fig. 7a) meets these requirements. The other calculated structures are shown in Fig. S1 of the ESI,<sup>†</sup> together with their 6-311G++(d,p) energetics. Their interactive 3-D structures are given in the ESI<sup>†</sup> structures file. Their energetic data calculated at the B3LYP-D3(BJ,abc)/ma-def2-TZVP level are listed in Table S1 (ESI<sup>†</sup>). The simulated spectra are shown in Fig. S2 (ESI<sup>†</sup>).

The most stable homochiral structure is built from the most stable monomers  $M_1$  and is what we shall call an “insertion” complex. The  $\text{O}_2\text{H}$  group of one of the monomers, called “guest” in what follows and denoted by the subscript “g”, inserts into the intramolecular hydrogen bond of the other monomer, called “host” and denoted by the subscript “h”. The intramolecular  $\text{O}_{1g}\text{H} \cdots \text{O}_{2g}$  hydrogen bond of the guest is retained while its  $\text{O}_{2g}\text{H} \cdots \pi$  contact is disrupted to the benefit of the strong intermolecular  $\text{O}_{2g}\text{H} \cdots \text{O}_{2h}$  interaction. The dangling  $\text{O}_{2h}\text{H}$  interacts with the aromatic ring of the guest. The intramolecular  $\text{O}_{1h}\text{H} \cdots \text{O}_{2h}$  hydrogen bond of the host is disrupted to the benefit of two strong intermolecular  $\text{O}_{2g}\text{H} \cdots \text{O}_{2h}$  and  $\text{O}_{1h}\text{H} \cdots \text{O}_{2g}$  interactions. The intramolecular hydrogen bond of the guest is hardly modified relative to the  $M_1$  monomer

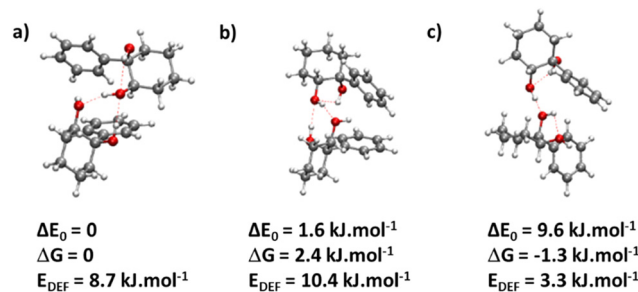


**Fig. 7** (a) Most stable homochiral dimer of *cis*-1-phenylcyclohexane-1,2-diol: insertion ( $M_1 + M_1$ ) (b) most stable heterochiral dimer of *cis*-1-phenylcyclohexane-1,2-diol (in terms of  $\Delta E_0$ ): insertion ( $M_1 + M_1$ ) (c) most stable heterochiral dimer of *cis*-1-phenylcyclohexane-1,2-diol (in terms of  $\Delta G$  at 300 K): addition  $\text{O}_2\text{H}_2 \rightarrow \text{O}_1(M_1 + M_1)$ . The red dotted lines show the  $\text{OH} \cdots \text{O}$  hydrogen bonds. The zero of the energy scale is at the most stable homochiral dimer.

( $\theta(\text{O}_{1g}\text{HO}_{2g}) = 116^\circ$  and  $d(\text{O}_{1g} \cdots \text{HO}_{2g}) = 2.19\text{ \AA}$  vs.  $115^\circ$  and  $2.22\text{ \AA}$ ). In contrast, the host undergoes strong deformation, which explains the large deformation energy ( $10.4\text{ kJ mol}^{-1}$ ). The experimental spectrum is readily assigned on the basis of this geometry (Fig. 6a and b). The bands observed at  $3344$  and  $3467\text{ cm}^{-1}$  are assigned to the  $\nu(\text{O}_{1h}\text{H})$  and  $\nu(\text{O}_{2g}\text{H})$ , respectively. The doublet at  $3554/3563\text{ cm}^{-1}$  is assigned to  $\nu(\text{O}_{2h}\text{H})$  and  $\nu(\text{O}_{1g}\text{H})$ , respectively.

More conformational diversity is observed for the heterochiral dimer and a different vibrational spectrum is obtained for the probe set on the transition located at  $257\text{ cm}^{-1}$  of the  $S_1 \leftarrow S_0$  transition origin or for the probe set on the  $S_1 \leftarrow S_0$  transition origin or any of the other bands. The spectrum with the probe set on the  $S_1 \leftarrow S_0$  origin (Fig. 6c) shows four transitions, at  $3380$ ,  $3516$ ,  $3555$  and  $3563\text{ cm}^{-1}$ . It is attributed to the most stable (at 0 K) calculated structure (Fig. 7b), which is very similar to the homochiral dimer described above. A similar insertion structure is calculated with similar hydrogen bonds, with a deformation energy of the same order as the corresponding homochiral complex. The spectrum simulated for this structure is in excellent agreement with the experimental findings (Fig. 6c and d). The assignments of the bands at  $3380$  and  $3516\text{ cm}^{-1}$  or the doublet at  $3555/3563\text{ cm}^{-1}$  parallel that of the homochiral dimer.

The spectrum obtained when probing the band at  $+257\text{ cm}^{-1}$  (band marked with an encircled asterisk in Fig. 5) shows a different pattern, with a smaller down-shift of the  $\nu(\text{OH})$  frequencies. Four bands appear at  $3428$ ,  $3513$ ,  $3542$ ,  $3603\text{ cm}^{-1}$ . Based on agreement between simulated and experimental frequencies, it is assigned to an addition complex (linear structure), which is high in energy at 0 K but predicted to become competitive at higher temperature (see Fig. 8 and Table S1, ESI<sup>†</sup>). The other calculated heterochiral structures are shown in Fig. S2 of the ESI,<sup>†</sup> together with their 6-311G++(d,p) energetics. Their interactive 3-D structures are given in the ESI<sup>†</sup> structures file. The addition complex is built from a  $M_1$  monomer acting as a donor, which adds to a  $M_1$  monomer *via* a strong intermolecular hydrogen bond. The donor and the acceptor will be denoted by the subscript “d” or “a”, respectively. They both keep their intramolecular hydrogen bond



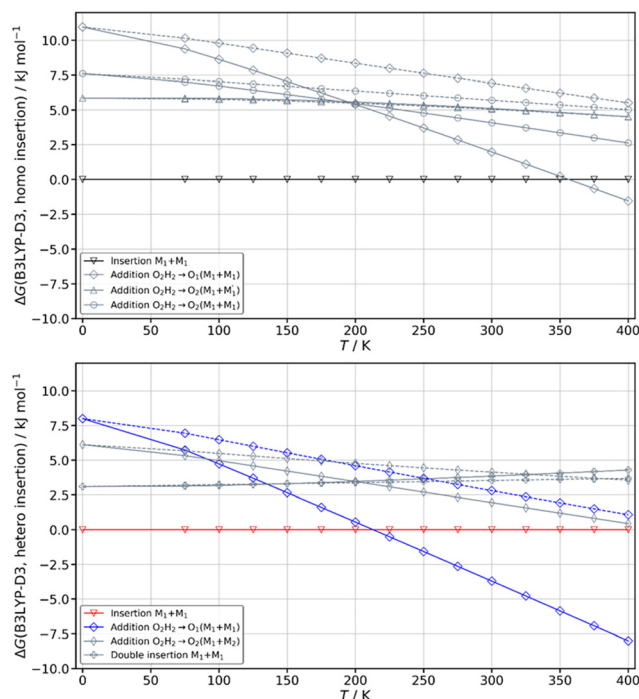


Fig. 8 Variation of the Gibbs energy of the most stable calculated complexes as a function of the temperature computed at the B3LYP-D3(BJ,abc)/ma-def2-TZVP level of theory. The zero of the scale is taken at the most stable insertion structure of each dimer. Solid lines indicate the use of the Rigid Rotor Harmonic Oscillator (RRHO) approximation while dashed lines indicate the use of Grimme's Quasi Rigid Rotor Harmonic Oscillator (QRRHO) approximation.

$\text{O}_1\text{H}\cdots\text{O}_2$  intact. Because the geometry of the monomer within the complex is very close to that of the bare monomers (no disruption of the intramolecular hydrogen bonds), the deformation energy is very low ( $3.3 \text{ kJ mol}^{-1}$ ). The dangling  $\text{O}_{2d}\text{H}$  of the donor is involved in a strong intermolecular  $\text{O}_{2d}\text{H}\cdots\text{O}_{1a}$  hydrogen bond while that of the acceptor is involved in the same  $\text{OH}\cdots\pi$  interaction as the monomer. There is a rather large uncertainty in energy ranking as the addition dimer is less stable by  $8.0 \text{ kJ mol}^{-1}$  in terms of  $\Delta E_0$  but more stable by  $3.7 \text{ kJ mol}^{-1}$  than the insertion heterodimer in terms of Gibbs energy at 300 K. This uncertainty mainly arises from the fact that the insertion complexes are tighter than addition complexes; the evolution of the Gibbs free energy as a function of the temperature is in favour of the latter as one can already see from the large discrepancy between  $\Delta G$  and  $\Delta E_0$  provided in Fig. 7. The temperature at which the complexes are formed in the out-of-equilibrium supersonic expansion is not known but the fact that we see both heterochiral complexes, the insertion one being dominant, seems to indicate that the temperature at which the complexes are formed is higher than 100 K (see Fig. 8). As expected for rigid complexes, the insertion and double insertion dimers show little variation of their relative  $\Delta G$  as a function of the temperature. This contrasts to the addition complexes, in particular the heterochiral addition  $\text{O}_2\text{H}_2 \rightarrow \text{O}_1 (\text{M}_1 + \text{M}_1)$  dimer to which one of the experimentally observed spectra is assigned. The observation of this dimer provides an indirect measurement of the jet conformational

temperature, which can be estimated at similar values using different basis set; a switch from ma-def2-TZVP to 6-311G++(d,p) would suggest a slightly different conformational temperature (175 K vs. 150 K). However, one should not overestimate the robustness of this estimate, as a different way of dealing with the entropy of very low frequency vibrations<sup>44</sup> would suggest very different conformational temperature. Resorting to the QRRHO corrections would result in a less realistic temperature above 300 K (dashed lines in Fig. 8).

(c) **Localisation of the electronic transitions.** Two chromophores are present in the dimer, which gives rise to two electronic transitions as observed in hydrogen-bound<sup>50</sup> or dispersion-bound dimers<sup>51</sup> of aromatic molecules as well as bichromophoric systems.<sup>36,49,52,53</sup> The difference in electronic density describing the  $\text{S}_1 \leftarrow \text{S}_0$  and  $\text{S}_2 \leftarrow \text{S}_0$  transitions is shown in Fig. 9. As expected from the presence of the benzene chromophore, these transitions are  $\pi\pi^*$  transitions localised on the aromatic rings. For both homochiral and heterochiral insertion dimers,  $\text{S}_1 \leftarrow \text{S}_0$  is located on the ring of the host. The higher-energy transition is located on the aromatic ring of the guest, which acts as an acceptor for the  $\text{OH}\cdots\pi$  interaction. This upshift of the electronic transition is due to the decrease of the electrostatic interactions upon electronic excitation, due to the weakening of the  $\text{OH}\cdots\pi$  hydrogen bond, and has been observed before.<sup>54–58</sup>

### 3. Comparison between homo and heterochiral dimers

A similar insertion structure is observed for both homochiral and heterochiral dimers, with similar hydrogen bonds and deformation energies. A structural difference lies in the fact that, due to the stereochemical constraints, the aromatic rings are facing each other in the heterochiral dimer while they are on opposite sides of the homochiral dimer. An increase in temperature strongly favours the addition dimers (see Fig. 8) because addition complexes are less rigid, which makes them favoured at high temperature, entropic effects being more

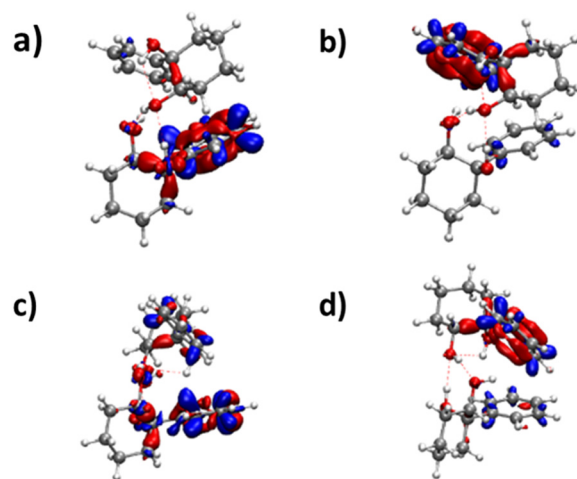


Fig. 9 Difference in electronic density for (a) the  $\text{S}_1 \leftarrow \text{S}_0$  (b)  $\text{S}_2 \leftarrow \text{S}_0$  transitions of the insertion homochiral dimer and (c) the  $\text{S}_1 \leftarrow \text{S}_0$  (d) the  $\text{S}_2 \leftarrow \text{S}_0$  transitions of the insertion heterochiral dimer.



important there than the intrinsic hydrogen bond strength. Still, the insertion dimer is the most stable structure for the homochiral dimer, at 0 K and 300 K alike. For the heterochiral complex, the addition dimer is strongly stabilised at 300 K (by 3.7 kJ mol<sup>-1</sup>) relative to the insertion. The same is obtained to a lesser extent (0.5 kJ mol<sup>-1</sup>) using the B3LYP-D3BJ/6-311G++(d,p) values. However, a larger stability of the addition relative to the insertion heterochiral dimer would be in contradiction with the more intense and numerous bands assigned to the latter in the REMPI spectrum. Assuming that the oscillator strength of the electronic transition and ionisation efficiency are identical for both heterochiral structures, these experimental findings would suggest a larger abundance of the insertion heterochiral dimer in our experimental conditions. Hence, the temperature at which the two heterochiral dimers are formed is likely lower than 300 K.

The calculated value of the chirodiastaltic energy is different whether  $\Delta E_0$  or  $\Delta G$  is considered (see Fig. 8 and Table S1, ESI<sup>†</sup>), and also depends on the level of theory used. Homochiral preference is obtained at 0 K whatever the method used;  $\Delta E_0(\text{hom-het})$  amounts to 1.6 kJ mol<sup>-1</sup> at the B3LYP-D3(BJ,abc)/ma-def2-TZVP level and 1.7 kJ mol<sup>-1</sup> for B3LYP-D3BJ/6-311G++(d,p), respectively. Note that when  $\Delta E_0$  is considered, the most stable homo- and heterochiral complexes are both insertion structures but when  $\Delta G$  at 300 K is considered the most stable heterochiral structure is the addition dimer that would energetically win over the homochiral dimer by 1.3 kJ mol<sup>-1</sup> at 300 K. Changing the basis set from ma-def2-TZVP to 6-311G++(d,p) reverses this trend and retrieves the homochiral preference (by 2.3 kJ mol<sup>-1</sup>) at 300 K.

The frequencies located on O<sub>2g</sub>H and O<sub>1h</sub>H are lower in the homochiral than the heterochiral dimer, suggesting stronger hydrogen bonds in the former. Non-covalent (NCI) calculations<sup>59,60</sup> indeed indicate a slightly larger electron density for the intermolecular hydrogen bonds of the homochiral dimer (0.199 and 0.177 vs. 0.197 and 0.175 for the heterochiral dimer). This observation is compatible with a larger stability of the homochiral dimer, although it should be taken with caution as stronger hydrogen bonds do not always correlate with an overall larger stability.<sup>61</sup> Introducing the QRRHO approximation allows retrieving a chirodiastaltic Gibbs free energy in favour of the homochiral dimer (1.8 kJ mol<sup>-1</sup>), and an insertion heterochiral complex more stable than the addition structure, but would suggest a conformational temperature in the jet close to room temperature. Still, there are concordant indications in favour of a homochiral preference, although each taken separately (energy at 0 K, relative intensities in the electronic spectrum, down shift of the  $\nu(\text{OH})$ ) is not sufficiently conclusive.

The heterochiral dimer shows more conformational flexibility than the homochiral one as it exists in two forms. A larger conformational flexibility has been observed already for the less stable configuration of chiral systems, for example heterochiral peptides, or protonated methyl tartrate dimers,<sup>52,62,63</sup> or the homochiral 1-indanol dimer.<sup>11</sup> A larger conformational flexibility of the homochiral adduct was observed as well for the *trans*-CD dimer for which the most stable calculated dimer is heterochiral.<sup>23</sup>

#### 4. Comparison with *cis*- and *trans*-1,2-cyclohexanediol

We shall now compare the structures described above to those obtained for similar systems, namely, *cis*- and *trans*-CD. The hydrogen bond patterns observed for the most stable dimers of the three systems at low temperature are sketched in Fig. 10. Further possible hydrogen bond patterns are sketched in Fig. S5 of the ESI.<sup>†</sup> The energetics of the *cis*-CD, *trans*-CD and *cis*-PCD dimers are summarised in Fig. 11.

The Raman spectrum of *cis*-CD,<sup>46</sup> taken with experimental conditions optimised for dimer formation, is shown in Fig. 12. It has one dominant band at 3419 cm<sup>-1</sup>, which is predicted to arise mainly from the most stable transiently heterochiral dimer, whereas the most likely similarly abundant transiently homochiral dimer is spread over several conformations and weaker transitions at lower and mostly at higher wavenumber. The lack of conformational selectivity prevents any further spectral assignment, but the calculations suggest that the homo- and heterochiral dimers have a very different hydrogen bond topology. Similar to *trans*-CD, a heterochiral quadruple insertion dimer is predicted to be the most stable dimer with other hetero- and homochiral dimers being significantly higher in energy, although not quite as pronounced as for *trans*-CD ( $\Delta E_0(\text{hom-het})$  for *cis*-CD is 3.8 kJ mol<sup>-1</sup> vs. 6.6 kJ mol<sup>-1</sup> for *trans*-CD at the B3LYP-D3/ma-def2-TZVP level). The analogy to *trans*-CD also holds for the homochiral dimers with the most stable ones being close in energy as well as structurally related. Of these four dimers a cyclic structure (two intermolecular and two intramolecular hydrogen bonds) is energetically favoured. The somewhat surprising similarity between *cis*-CD and *trans*-CD can be explained by the fact that the O-C-C-O dihedral angles of the diol subunit are still quite similar. Hence, the fact that the chiral preference in *cis*-PCD is inverted can most likely be attributed to the introduction of the phenyl group. The most stable homochiral cyclic (double addition) pattern contrasts to that at play in the homochiral *cis*-PCD dimer that involves two intermolecular and one intramolecular OH...O interactions. This is because the aromatic ring electrons compete with the oxygen as a hydrogen bond acceptor; both homochiral and heterochiral *cis*-PCD insertion dimers involve indeed an OH... $\pi$  interaction.

Calculations confirm that there is little similarity between the most stable complexes of *cis*-PCD and *cis*-CD in a

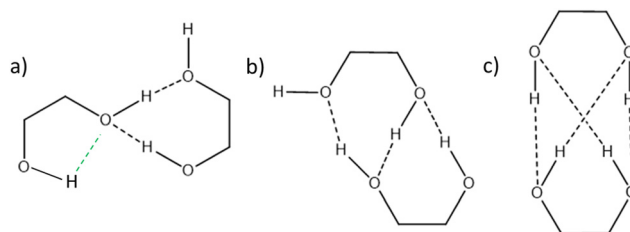


Fig. 10 Hydrogen bond pattern observed in (a) the most stable (in terms of  $\Delta E_0$ ) homochiral or heterochiral dimer of *cis*-PCD (insertion) (b) the most stable homochiral dimer of *trans*- or *cis*-CD (double insertion) (c) the most stable heterochiral dimer of *trans*- or *cis*-CD (quadruple insertion).







**Fig. 11** Comparison between the zero-point corrected energy landscape of the heterochiral dimers of *cis*-PCD (outer left) and *cis*-CD (middle left) as well as the homochiral dimers of *cis*-CD (middle right) and *cis*-PCD (outer right) up to 10 kJ mol<sup>-1</sup>. Energy levels of homo-chiral and heterochiral dimers are shown in red and black, respectively. The three dashed-dotted energy levels of *cis*-PCD correspond to dimers which have been assigned experimentally. *cis*-CD conformers that converge to a corresponding conformer of *cis*-PCD after substitution by a phenyl and *vice versa* are linked by dashed lines. Additionally, the five most stable hetero- and homochiral conformers of *trans*-CD are shown and analogous *cis*-CD and *trans*-CD conformers are connected by dashed lines. Because the most stable (heterochiral, quadruple-insertion) structures are aligned at energy 0 for *cis*- and *trans*-CD, the downward slopes of the other *trans*-CD structures towards *cis*-CD show that the *cis* arrangement selectively destabilises this quadruple-insertion motif. The zero-point corrected energies have been calculated at the B3LYP-D3(BJ,abc)/ma-def2-TZVP level of theory. 2× indicates that two conformers are isoenergetic.

10 kJ mol<sup>-1</sup> window (see Fig. 11 and Fig. 13). The conformational locking induced by the phenyl on the *cis*-PCD monomer also exists for its dimers, as shown by the much higher density of structures for *cis*-CD. The insertion dimer is indeed the only homochiral stable structure in a 5 kJ mol<sup>-1</sup> window at low temperature (see Fig. 8). In *cis*-PCD, the chirodiastaltic energy favours the homochiral complex. This contrasts to what is calculated for *trans*-CD or *cis*-CD for which the most stable calculated dimer is the heterochiral one ( $\Delta E_0 = 6.6$  kJ mol<sup>-1</sup> and 3.8 kJ mol<sup>-1</sup>, respectively, at the B3LYP-D3/ma-def2-TZVP level) due to its structure (quadruple insertion) that optimises the number of hydrogen bonds.

The energetics sketched in Fig. 11 illustrate the main points of the comparison between the different systems. The lesser density of structures for *cis*-PCD, independently of chirality, illustrates the conformational locking induced by the aromatic ring. Both *cis*- and *trans*-CD show heterochiral preference with a quadruple insertion structure, which contrast with *cis*-PCD that shows homochiral preference. On a common energy scale where the most stable dimer irrespective of relative chirality is aligned, the most stable homochiral dimer of *cis*-CD is destabilised by  $\sim 5$  kJ mol<sup>-1</sup> when adding an aromatic ring, because of the steric hindrance brought by the latter.



**Fig. 12** Comparison between the experimental (top) and simulated (bottom) Raman spectrum of *cis*-CD in 1.4 bar of helium. The saturator (365 K) and nozzle (385 K) temperatures have been optimised for dimer formation. Reasonable agreement can be found between the simulation and the experiment. See Fig. 13 for depiction of the corresponding structures. For the simulation, it is assumed that homo- and heterochiral dimers are formed with equal likelihood. Furthermore, the three most stable homo-dimers are assumed to be isoenergetic and therefore the homo population is equally spread among them. Since the most stable heterochiral dimer is energetically unrivalled one arrives at statistical weights of 1:1/3:1/3:1/3 (quadruple insertion: cyclic: double insertion: double insertion A). Such an approach was previously successfully used for *trans*-CD. The simulation assumes Gaussian profile with a FWHM of 8 cm<sup>-1</sup>.

Conversely, the most stable homochiral *cis*-PCD dimer is stabilised by  $\sim 9$  kJ mol<sup>-1</sup> relative to the equivalent in CD.

## 5. Structure of the solid state

(*R,R*) enantiopure and racemic *cis*-PCD samples have been dissolved in ethanol and allowed to crystallise slowly, resulting in long needle-shaped crystals. The X-ray diffraction pattern of both samples has been recorded following the procedure described in the ESI.† The enantiopure crystal belongs to the monoclinic Sohncke group C2, characterised by a two-fold rotation axis and a two-fold screw axis. The unit cell, displayed in Fig. 14a, contains two non-equivalent monomers interacting *via* two intermolecular hydrogen bonds, in what can be called an addition structure. The superimposed structure of the two monomers are shown in Fig. S6 of the ESI.† The structure of one of the monomers is close to M<sub>1</sub>, with an O<sub>1</sub>H<sub>1</sub>...O<sub>2</sub> hydrogen bond, while the other is close to M<sub>2</sub> with an O<sub>2</sub>H<sub>2</sub>...O<sub>1</sub> interaction. The dangling OH of each monomer binds to the monomer of same nature in a neighbouring dimer, resulting in long hydrogen-bonded chains that explain the needle-like appearance of the crystal (Fig. 14b). The racemic *cis*-PCD is a conglomerate composed of a 50/50 mixture of (*R,R*) and (*S,S*) crystals. In the solid phase as well, homochiral preference is therefore observed. This contrasts to *trans*-CD whose racemic crystal crystallises as a racemate in the C2/c space group, which contains an inversion centre.<sup>24</sup> The asymmetric unit is a *trans*-CD monomer that converts into its enantiomer *via* the inversion operation, resulting in a similar addition dimer, with monomers in a geometry intermediate between M and M' (O<sub>1</sub>O<sub>2</sub>H angle of 131°).



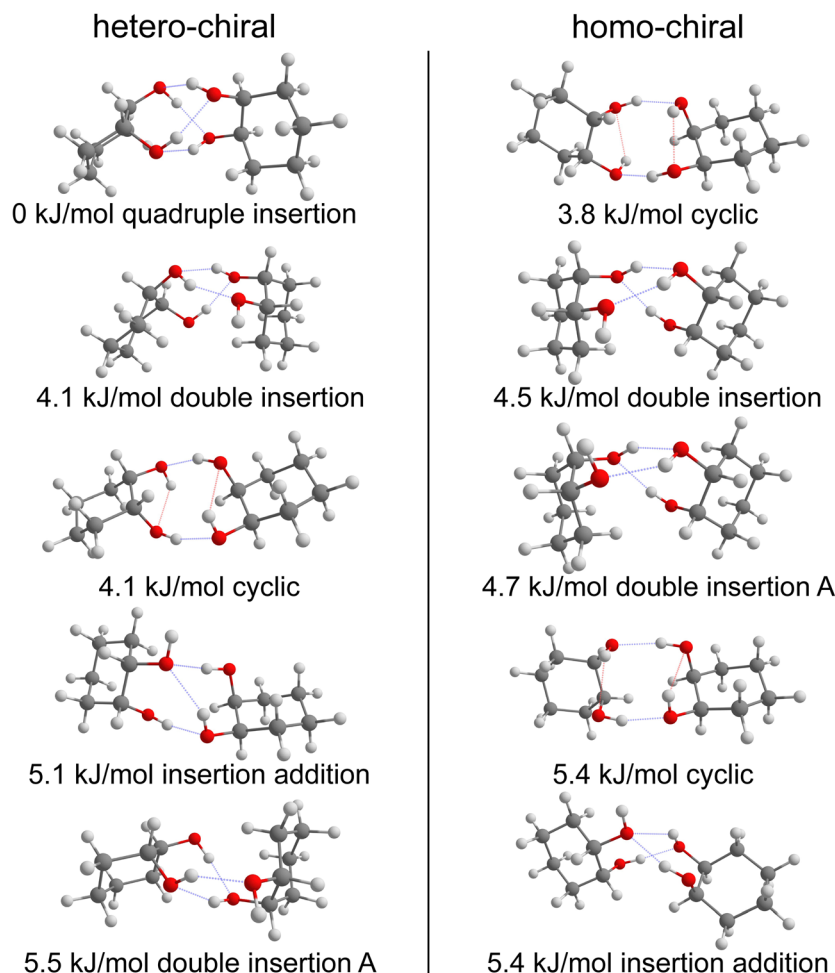


Fig. 13 Five most stable hetero- (left) and homo-chiral (right) dimers of *cis*-CD, respectively. The zero-point corrected energies at the B3LYP-D3(BJ,abc)/ma-def2-TZVP level are shown. Intermolecular hydrogen bonds are highlighted in blue and intramolecular ones in red.



Fig. 14 (a) Unit cell of the *cis*-PCD crystal (b) array of hydrogen bonded chains.

## Conclusion

The spectroscopic study of the chiral diol *cis*-PCD and its dimer emphasises several differences relative to the previously studied permanently chiral *trans*-CD and the transiently chiral *cis*-CD diols further explored in this work. First, the steric

hindrance due to the bulky phenyl ring, in addition to its hydrogen bond acceptor capability that allows formation of an OH... $\pi$  hydrogen bond, induces conformational locking in *cis*-PCD relative to *cis*-CD and decreases the number of populated conformers. *cis*-PCD exists therefore in one conformer only under supersonic jet conditions. The most stable structure of both homochiral and heterochiral dimers of *cis*-PCD at low temperature is an insertion structure, with the O<sub>2</sub>H group of the guest inserted in the intramolecular hydrogen bond of the host. With increasing temperature, competition by more floppy addition complexes sets in, first in the heterochiral case, as also evidenced by experiment. The recently observed tunneling splitting present in one of the homo dimers of *trans*-CD should not be of concern for *cis*-PCD given the large structural changes relative to *trans*-CD that do not readily allow for a conversion between equivalent conformers.<sup>64</sup> The homochiral preference observed for cold *cis*-PCD contrasts to what was observed in *trans*-CD and *cis*-CD for which the predicted heterochiral preference is explained by the formation of an outstandingly stable heterochiral dimer that optimises the number of possible hydrogen bonds *via* a quadruple insertion structure. Due to



the strong similarities between *cis*-CD and *trans*-CD, it is clear that the changes in clustering propensity of *cis*-PCD are due to the presence of the phenyl substituent rather than the consequences of *cis-trans* isomerism. These findings at the molecular level parallel those in the crystal, as racemic *cis*-PCD is a conglomerate while *trans*-CD is a racemate.

## Conflicts of interest

There are no conflicts to declare.

## Acknowledgements

Funding by the Deutsche Forschungsgemeinschaft (DFG, German Research Foundation) – 389479699/GRK2455 and 405832858 for computational resources is acknowledged. We acknowledge the computing centre MésoLUM managed by ISMO (UMR8214) and LPGP (UMR8578), University Paris-Saclay (France).

## References

- I. Myrgorodska, C. Meinert, S. V. Hoffmann, N. C. Jones, L. Nahon and U. J. Meierhenrich, *ChemPlusChem*, 2017, **82**, 74–87.
- J. Podlech, *Cell. Mol. Life Sci.*, 2001, **58**, 44–60.
- W. A. Bonner, *Origins of Life and Evolution of the Biosphere*, 1995, vol. 25, pp. 175–190.
- R. Sudha and M. F. Jarrold, *J. Phys. Chem. B*, 2005, **109**, 11777–11780.
- T. Rekis, *Acta Crystallogr., Sect. B: Struct. Sci., Cryst. Eng. Mater.*, 2020, **76**, 307–315.
- C. Brandel, S. Petit, Y. Cartigny and G. Coquerel, *Curr. Pharm. Des.*, 2016, **22**, 4929–4941.
- A. Otero-de-la-Roza, J. E. Hein and E. R. Johnson, *Cryst. Growth Des.*, 2016, **16**, 6055–6059.
- L. Pasteur, *C. R. Acad. Sci.*, 1853, **37**, 162.
- A. Zehnacker, *Int. Rev. Phys. Chem.*, 2014, **33**, 151–207.
- A. Zehnacker and M. A. Suhm, *Angew. Chem., Int. Ed.*, 2008, **47**, 6970–6992.
- J. Altnoeder, A. Bouchet, J. J. Lee, K. E. Otto, M. A. Suhm and A. Zehnacker-Rentien, *Phys. Chem. Chem. Phys.*, 2013, **15**, 10167–10180.
- X. C. Liu, N. Borho and Y. J. Xu, *Chem. – Eur. J.*, 2009, **15**, 270–277.
- W. H. Pirkle and T. C. Pochapsky, *Chem. Rev.*, 1989, **89**, 347–362.
- N. Borho and M. A. Suhm, *Org. Biomol. Chem.*, 2003, **1**, 4351–4358.
- N. Borho and M. A. Suhm, *Phys. Chem. Chem. Phys.*, 2004, **6**, 2885–2890.
- T. B. Adler, N. Borho, M. Reiher and M. A. Suhm, *Angew. Chem., Int. Ed.*, 2006, **45**, 3440–3445.
- A. Bouchet, J. Klyne, S.-I. Ishiuchi, O. Dopfer, M. Fujii and A. Zehnacker, *Phys. Chem. Chem. Phys.*, 2018, **20**, 12430–12443.
- D. F. Plusquellic, F. J. Lovas, B. H. Pate, J. L. Neill, M. T. Muckle and A. J. Remijan, *J. Phys. Chem. A*, 2009, **113**, 12911–12918.
- F. Kollipost, K. E. Otto and M. A. Suhm, *Angew. Chem., Int. Ed.*, 2016, **55**, 4591–4595.
- P. Asselin, B. Madebene, P. Soulard, R. Georges, M. Goubet, T. R. Huet, O. Pirali and A. Zehnacker-Rentien, *J. Chem. Phys.*, 2016, 145.
- R. Medel, A. Camiruaga, R. T. Saragi, P. Pinacho, C. Perez, M. Schnell, A. Lesarri, M. A. Suhm and J. A. Fernandez, *Phys. Chem. Chem. Phys.*, 2021, **23**, 23610–23624.
- T. Scharge, T. Haber and M. A. Suhm, *Phys. Chem. Chem. Phys.*, 2006, **8**, 4664–4667.
- B. Hartwig, M. Lange, A. Poblitzki, R. Medel, A. Zehnacker and M. A. Suhm, *Phys. Chem. Chem. Phys.*, 2020, **22**, 1122–1136.
- S. Jahnigen, A. Zehnacker and R. Vuilleumier, *J. Phys. Chem. Lett.*, 2021, **12**, 7213–7220.
- N. Seurre, J. Sepiol, K. Le Barbu-Debus, F. Lahmani and A. Zehnacker-Rentien, *Phys. Chem. Chem. Phys.*, 2004, **6**, 2867–2877.
- N. Seurre, J. Sepiol, F. Lahmani, A. Zehnacker-Rentien and K. Le Barbu-Debus, *Phys. Chem. Chem. Phys.*, 2004, **6**, 4658–4664.
- R. Medel and M. A. Suhm, *Phys. Chem. Chem. Phys.*, 2020, **22**, 25538–25551.
- D. Scuderi, K. Le Barbu-Debus and A. Zehnacker, *Phys. Chem. Chem. Phys.*, 2011, **13**, 17916–17929.
- R. N. Pribble and T. S. Zwier, *Science*, 1994, **265**, 75–79.
- S. Tanabe, T. Ebata, M. Fujii and N. Mikami, *Chem. Phys. Lett.*, 1993, **215**, 347–352.
- A. Sen, A. Bouchet, V. Lepère, K. Le Barbu-Debus, D. Scuderi, F. Piuze and A. Zehnacker-Rentien, *J. Phys. Chem. A*, 2012, **116**, 8334–8344.
- R. A. Marta, R. H. Wu, K. R. Eldridge, J. K. Martens and T. B. McMahon, *Int. J. Mass Spectrom.*, 2010, **297**, 76–84.
- M. J. Frisch, J. A. Pople and J. S. Binkley, *J. Chem. Phys.*, 1984, **80**, 3265–3269.
- S. Grimme, J. Antony, S. Ehrlich and H. Krieg, *J. Chem. Phys.*, 2010, **132**, 154104.
- S. Grimme, S. Ehrlich and L. Goerigk, *J. Comput. Chem.*, 2011, **32**, 1456–1465.
- F. BenNasr, A. Pérez-Mellor, I. Alata, V. Lepere, N. E. Jaidane and A. Zehnacker, *Faraday Discuss.*, 2018, **212**, 399–419.
- M. D. Halls, J. Velkovski and H. B. Schlegel, *Theor. Chem. Acc.*, 2001, **105**, 413.
- K. Le Barbu-Debus, in *Chiral Recognition in the Gas Phase*, ed. A. Zehnacker, CRC Press Taylor and Francis, Boca Raton, 2010, ch. 4, pp. 47–59.
- N. Borho, M. A. Suhm, K. Le Barbu-Debus and A. Zehnacker, *Phys. Chem. Chem. Phys.*, 2006, **8**, 4449–4460.
- M. J. Frisch, G. W. Trucks, H. B. Schlegel, G. E. Scuseria, M. A. Robb, J. R. Cheeseman, G. Scalmani, V. Barone, G. A. Petersson, H. Nakatsuji, X. Li, M. Caricato, A. V. Marenich, J. Bloino, B. G. Janesko, R. Gomperts, B. Mennucci, H. P. Hratchian, J. V. Ortiz, A. F. Izmaylov, J. L. Sonnenberg Williams, F. Ding, F. Lipparini, F. Egidi, J. Goings, B. Peng, A. Petrone, T. Henderson,



- D. Ranasinghe, V. G. Zakrzewski, J. Gao, N. Rega, G. Zheng, W. Liang, M. Hada, M. Ehara, K. Toyota, R. Fukuda, J. Hasegawa, M. Ishida, T. Nakajima, Y. Honda, O. Kitao, H. Nakai, T. Vreven, K. Throssell, J. A. Montgomery Jr., J. E. Peralta, F. Ogliaro, M. J. Bearpark, J. J. Heyd, E. N. Brothers, K. N. Kudin, V. N. Staroverov, T. A. Keith, R. Kobayashi, J. Normand, K. Raghavachari, A. P. Rendell, J. C. Burant, S. S. Iyengar, J. Tomasi, M. Cossi, J. M. Millam, M. Klene, C. Adamo, R. Cammi, J. W. Ochterski, R. L. Martin, K. Morokuma, O. Farkas, J. B. Foresman and D. J. Fox, 2016.
- 41 J. Zheng, X. Xu and D. G. Truhlar, *Theor. Chem. Acc.*, 2011, **128**, 295–305.
- 42 F. Weigend and R. Ahlrichs, *Phys. Chem. Chem. Phys.*, 2005, **7**, 3297–3305.
- 43 F. Neese, *Wiley Interdiscip. Rev.: Comput. Mol. Sci.*, 2017, **8**, e1327.
- 44 S. Grimme, *Chem. – Eur. J.*, 2012, **18**, 9955–9964.
- 45 R. S. Ruoff, T. D. Klots, T. Emilsson and H. S. Gutowsky, *J. Chem. Phys.*, 1990, **93**, 3142–3150.
- 46 B. Hartwig and M. A. Suhm, *Phys. Chem. Chem. Phys.*, 2021, **23**, 21623–21640.
- 47 M. Broquier, F. Lahmani, A. Zehnacker-Rentien, V. Brenner, P. Millie and A. Peremans, *J. Phys. Chem. A*, 2001, **105**, 6841–6850.
- 48 R. W. Larsen and M. A. Suhm, *J. Chem. Phys.*, 2006, **125**, 154314.
- 49 A. Zehnacker, F. Lahmani, E. Breheret, J. P. Desvergne, H. BouasLaurent, A. Germain, V. Brenner and P. Millie, *Chem. Phys.*, 1996, **208**, 243–257.
- 50 N. M. Kidwell, B. Nebgen, L. V. Slipchenko and T. S. Zwier, *J. Chem. Phys.*, 2019, **151**, 084313.
- 51 U. Erlekam, M. Frankowski, G. von Helden and G. Meijer, *Phys. Chem. Chem. Phys.*, 2007, **9**, 3786–3789.
- 52 J. Dupont, R. Guillot, V. Lepère and A. Zehnacker, *J. Mol. Struct.*, 2022, **1262**, 133059.
- 53 A. Pérez-Mellor, I. Alata, V. Lepere and A. Zehnacker, *J. Mol. Spectrosc.*, 2018, **349**, 71–84.
- 54 K. Le Barbu, F. Lahmani and A. Zehnacker-Rentien, *J. Phys. Chem. A*, 2002, **106**, 6271–6278.
- 55 K. Le Barbu, F. Lahmani, M. Mons, M. Broquier and A. Zehnacker, *Phys. Chem. Chem. Phys.*, 2001, **3**, 4684–4688.
- 56 C. E. H. Dessent, W. D. Geppert, S. Ullrich and K. Muller-Dethlefs, *Chem. Phys. Lett.*, 2000, **319**, 375–384.
- 57 M. Mons, I. Dimicoli, B. Tardivel, F. Piuze, V. Brenner and P. Millie, *J. Phys. Chem. A*, 1999, **103**, 9958–9965.
- 58 C. J. Gruenloh, F. C. Hagemester, J. R. Carney and T. S. Zwier, *J. Phys. Chem. A*, 1999, **103**, 503–513.
- 59 R. Chaudret, B. d Courcy, J. Contreras-Garcia, E. Gloaguen, A. Zehnacker-Rentien, M. Mons and J. P. Piquemal, *Phys. Chem. Chem. Phys.*, 2014, **16**, 9876–9891.
- 60 E. R. Johnson, S. Keinan, P. Mori-Sanchez, J. Contreras-Garcia, A. J. Cohen and W. Yang, *J. Am. Chem. Soc.*, 2010, **132**, 6498–6506.
- 61 P. Hurtado, F. Gamez, S. Hamad, B. Martinez-Haya, J. D. Steill and J. Oomens, *J. Chem. Phys.*, 2012, 136.
- 62 V. Lepere, K. Le Barbu-Debus, C. Clavaguera, D. Scuderi, G. Piani, A.-L. Simon, F. Chiro, L. MacAleese, P. Dugourd and A. Zehnacker, *Phys. Chem. Chem. Phys.*, 2016, **18**, 1807–1817.
- 63 K. Le Barbu-Debus, D. Scuderi, V. Lepere and A. Zehnacker, *J. Mol. Struct.*, 2020, **1205**, 127583.
- 64 F. Xie, W. Sun, B. Hartwig, D. A. Obenchain and M. Schnell, *Angew. Chem., Int. Ed.*, 2023, **62**(37), e202308273.

